Design of Small-Size Lithium-Battery Based Electromagnetic Induction Heating Control System

Yuanjie Liang , Shihao Song , Bocheng Xu , Zhuangzhuang Li , Xuelin Li , Zonglai Mo * , and Jun Li *

Posted Date: 31 July 2024

doi: 10.20944/preprints202407.2474.v1

Keywords: Electromagnetic Induction Heating; Lithium-battery heating; full bridge inverter; temperature control

Article

Design of Small-Size Lithium-Battery Based Electromagnetic Induction Heating Control System

Yuanjie Liang [1], Shihao Song [2], Bocheng Xu [3], Zhuangzhuang Li [1], Xuelin Li [1], Zonglai Mo [1,*] and Jun Li [1,*]

[1] School of Mechanical Engineering, Nanjing University of Science and Technology, Nanjing 210000, China;
[2] Qingdao Yizhong Technology Co. Ltd., Qingdao 266021, China
[3] Shandong Special Equipment Inspection and Research Institute Group Co., Ltd., Jinan 250101, China
* Correspondence: z.mo@njust.edu.cn 12018089@njust.edu.cn

Abstract: This paper presents design and optimization of a small-size electromagnetic induction heating control system powered by a 3.7V-900mAh lithium battery and featuring an LC series resonant full bridge inverter circuit, which can be used in small size materials heating applications, such as micro medical devices. The effects of resonant capacitance, inductor wire diameter, heating tube material and wall thickness are studied to maximize the heating rate of the workpiece and meantime reduce the temperature rise of the NMOS transistor. The optimal circuit configuration meeting the design requirements was finally identified via comparing the operational parameters and NMOS transistor loss under different circuit conditions. The validation experiments were conducted on a designed electromagnetic induction smoking devices. The results indicate that under an output current of 4.6A, the heating tube can reach up to the temperature target of 250°C within 11 seconds, and all NMOS transistors stay below 50°C in a 5 minutes heating process.

Keywords: Electromagnetic Induction Heating; Lithium-battery heating; full bridge inverter; temperature control

1. Introduction

Compared to traditional resistive heating, electromagnetic induction heating offers many advantages such as high efficiency, rapid heating, precise power control, and localized heating, and high safety due to non-contact. Currently, induction heating applications are primarily adopted on high-voltage, large-scale heating equipment in metal processing industries, medical fields, and cooking devices, such as high-power metal smelting[1–4],household induction stove optimization[5–7],or non-contact heating of internal metal implants [8–10].

In these large-scale devices, the electromagnetic induction heating control system is mainly divided into two parts: a rectification circuit and an inverter circuit composed of n-channel NMOS (NMOS) transistors, a heating coil, and a resonant capacitor. The rectification circuit converts the mains frequency AC power into DC power, while the inverter circuit converts the DC power into AC power of the required specific frequency and performs heating of the workpiece through energy conversion. The inverter can be categorized into two types: series resonant inverters (SRI)[11–13] and parallel resonant inverters (PRI) [14–16]. Among which, the SRI is a more cost-effective inversion scheme, offering a wider range of power adjustment options and being more suitable for applications that require frequent startups.

However, for the SRI circuit, load impedance matching is often required to ensure that the power output is suitable, which typically necessitates a transformer[17]. And the physical size and design complexity of transformers greatly increases the overall design difficulty of the system. Currently, the Inductor-Inductor-Capacitor (LLC) circuit[18–20] is commonly used to address this issue. It adds a matching inductor to replace the transformer on the basis of the Inductor-Capacitor (LC) circuit, and the inductor is typically larger than that of the heating inductor coil, which also leads to the increase of the overall system size. Due to the requirements for load impedance matching and the

 doi:10.20944/preprints202407.2474.v1

presence of the rectification circuit, the size of current electromagnetic induction heating devices is usually quite large, which limits the application of induction heating technology.

Soft switching means that the voltage or current at the drain-source level of the switching tube is zero at the instant of turn-on and turn-off, which is called zero-voltage switching (ZVS)[21–23] and zero-current switching (ZCS)[24–26], respectively, which is very advantageous for reducing the NMOS loss in medium- and high-frequency inverter circuits. Soft switching is highly related to NMOS losses, which usually cannot be avoided. Especially, it is more obvious in the miniaturization design of equipment. This is mainly due to the turn-on-loss caused by its own on-resistance and other parameters in the turn-on phase, and the turn-off-loss caused by the voltage and current of drain and source which can not disappear instantaneously at the same time when the NMOS is turned off[27–29]. For the same loss power, NMOS with small package size will have a larger temperature rise due to limited heat dissipation performance, which will also reduce the safety of the system and the heating efficiency of the system. Therefore, miniaturization design puts forward higher requirements for the optimization of NMOS loss.

In this paper, a small-size full-bridge LC series resonant circuit is used to realize the soft switching of NMOS in the resonant state. A composite power regulation method of phase shift-frequency regulation is proposed, where the phase shift process adjusts the duty cycle of the NMOS driving pulse, and the frequency regulation process locks the phase difference between the voltage and the current in the inverter circuit. This method simultaneously realizes power regulation, automatic tracking of target phase, zero-current turn-on of NMOS, and simplification of the hardware circuit. Compared to pulse density modulation (PDM)[30–32], it is more suitable for small current applications. And compared with frequency modulation (PFM)[33–35]and Phase-Shift Modulation (PSM)[36–38], it reduces the source of NMOS losses, which makes it easier to optimize the losses. Finally, to improve the performance of the control system, the influence of circuit parameters including resonant capacitance value, the wire diameter of the induction heating coil, the material and wall thickness of the heating tube on the performance of the heating system was studied through experiments. Finally, an ideal parameter combination of heating efficiency and energy loss of NMOS was determined.

2. Principles and Methods

2.1. Principle of Full-Bridge LC Series Resonant Electromagnetic Induction Heating

Figure 1 shows the electromagnetic induction heating control system commonly used in industry, which consists of a rectifier circuit and an inverter circuit. The rectifier circuit converts the industrial frequency alternating current (AC) into direct current (DC), and the inverter circuit adopts the circuit structure of full-bridge LLC series resonance, which realizes the inversion of voltage by controlling the two diagonal groups of NMOS to turn on and off alternately. The inversion process refers to the process of transforming a DC voltage into a certain frequency AC voltage. However, the high current with a high-frequency passed through LS usually needs a large size and not suitable for application in small induction heating devices powered by portable lithium batteries. In order to simplify the circuit, a simple full-bridge LC series resonant circuit structure is used in this paper, and the value of R in **Figure 1** can be adjusted via the inverter frequency, thus achieving the load impedance matching.

Preprints.org (www.preprints.org) | NOT PEER-REVIEWED | Posted: 31 July 2024 doi:10.20944/preprints202407.2474.v1

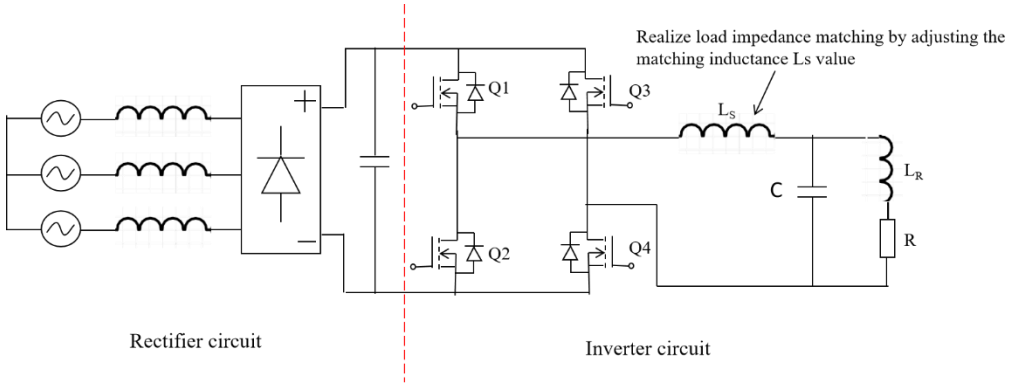

Figure 1. Structure of full-bridge LLC series resonant circuit for industrial induction heating control system.

Figure 2(a) shows the structure of the miniaturized induction heating control system. Its structure is mainly divided into two parts: the DC side and the inverter side, where the DC side is the battery side, and the inverter side referring to the inverter circuit side with AC voltage output. U_{BAT} represents the 3.7V lithium battery supply voltage, and Q1 to Q4 are NMOSs controlled by four independent square wave pulse signals from MCU. L_{eq} denotes the equivalent inductance of the inverter circuit, R_{eq} represents the equivalent resistance of the inverter circuit, C is the resonant capacitor of the circuit. By controlling two diagonal groups of NMOS, named Q1,Q4 and Q2,Q3, respectively, alternately turn on and off the lithium battery output DC into AC. The inverter frequency can be adjusted via the frequency control of the NMOSs to achieve the load impedance matching.

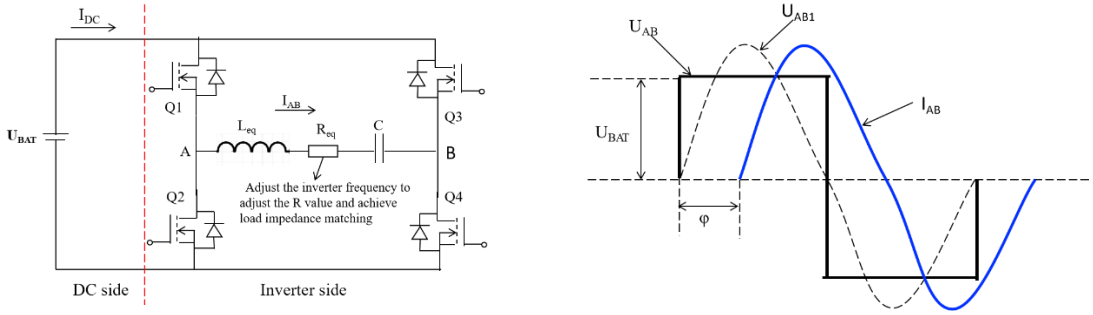

(**a**) (**b**)

Figure 2. (**a**) Structure of full-bridge LC series resonant circuit for small induction heating control system.(**b**) The waveform when the U_{AB} duty cycle is 50% and the power factor angle is φ.

Figure 2(b) shows a schematic diagram of the waveforms associated with the circuit. U_{AB} is the inverter voltage between points A and B. U_{AB1} is the fundamental component of the inverter voltage, with a frequency equal to the inverter frequency, and determines the inverter current. I_{DC} is the direct current from the battery and serves as a monitor for the circuit's status. I_{AB} is the sinusoidal current on the inverter side, and φ represents the phase difference, or power factor angle, between the inverter voltage and current.

In a full-bridge LC series resonant control system, the effective value of the fundamental component of the output voltage on the inverter side can be calculated:

$$U_{AB1} = \frac{4U_{DC}}{\sqrt{2}\cdot\pi} = \frac{2\sqrt{2}\cdot U_{DC}}{\pi} \quad (1)$$

where U_{DC} is the output voltage of the battery U_{BAT}.

The impedance of the inverter circuit is:

 doi:10.20944/preprints202407.2474.v1

$$\cos\varphi = \frac{R_{eq}}{Z} = \frac{R_{eq}}{\sqrt{{R_{eq}}^2 + \left(\omega L - \frac{1}{\omega C}\right)^2}} \tag{2}$$

where ω is the inverter angular frequency, φ is the power factor angle of the resonant circuit.

Effective value of the inverter side output current:

$$I_{AB} = \frac{U_{AB}}{Z} \tag{3}$$

Inverter side output power:

$$P_{AB} = U_{AB} \cdot I_{AB} \cdot \cos\varphi = \frac{8{U_{DC}}^2}{\pi^2 \cdot R} \cdot (\cos\varphi)^2 \tag{4}$$

When the inverter side frequency f equals the resonant frequency of the LC series circuit

$$\omega = \omega_0, \quad f = f_0 = \frac{1}{2\pi \cdot \sqrt{L_{eq}C}} \tag{3}$$

At this frequency, the power factor angle of the resonant circuit is 0, meaning that the inductive reactance and capacitive reactance cancel each other out, resulting in a minimum total impedance equal to the equivalent resistance R_{eq}. The current in the resonant circuit reaches its maximum value I_{AB0}.

$$\varphi = 0, \quad \cos\varphi = 1 \tag{7}$$

$$Z = R_{eq} \tag{8}$$

$$I_{AB0} = \frac{U_{AB}}{R_{eq}} \tag{9}$$

At this point, the voltage across the inductor coil and the resonant capacitor is

$$U_L = U_C = jQU_{AB} \tag{10}$$

where Q is the quality factor of the resonant circuit, given by:

$$Q = \frac{\omega_0 \cdot L}{R_{eq}} = \frac{1}{R_{eq}} \cdot \sqrt{\frac{L_{eq}}{C}} \tag{11}$$

According to Equation (8), at the resonant frequency f_0, the voltages across the inductor and capacitor terminals are equal in magnitude but opposite in direction, thus canceling each other out. This ensures that the voltage across U_{AB1} is effectively applied across the equivalent resistance R_{eq}. At this frequency, the voltage across the inductor and capacitor terminals is Q times the root mean square value of the fundamental inverter side voltage U_{AB1}. The quality factor Q is an important parameter of the LC resonant circuit. A higher Q value indicates greater sensitivity of the circuit to frequency variations. In the design of heating systems, as the system transitions from the heating stage to the temperature holding stage, the frequency gradually increases. During this transition, a high Q value effectively suppresses the increase in frequency, thereby reducing the NMOS losses of the transistor.

2.2. Low-Voltage Powered Small-size Electromagnetic Induction Heating Control System Structure and Circuit Principles

Figure 3(a) shows the overall structural framework of the small induction heating control system, and **Figure 3(b)** shows the layout of the PCB circuit board for the specific application of this structure in the design of heating non-combustible smokers. The PCB circuit board has a length of 84 mm and a width of 23 mm, and it is mainly divided into two modules, temperature control and frequency modulation (FM) phase-locked control. The temperature control process requires power

 doi:10.20944/preprints202407.2474.v1

regulation, and power regulation requires FM phase-locked control. Therefore, during the system operation, the two modules coordinate with each other to control the duty cycle and frequency of the NMOS drive signal respectively. The NMOSs are controlled through the half-bridge driver chip IR2101S, where the MCU signal input into.

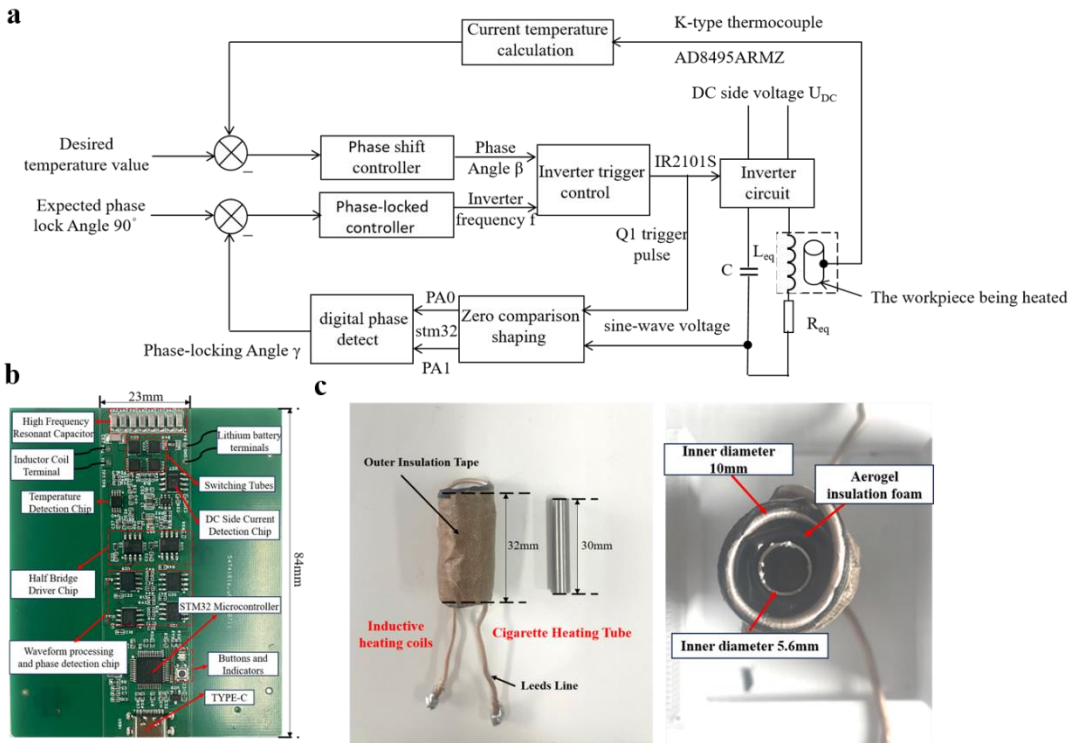

Figure 3. (**a**)Small electromagnetic induction heating control system overall structural frame (**b**) Heating non-combustible vape control system PCB circuit boards.(**c**)Relative positions and dimensions of induction coils, heating tubes and temperature holding layers.

In the temperature control module, a K-type thermocouple and the AD8495ARMZ chip are used to collect temperature data from the heating tube. The difference between the collected current temperature and the target temperature is then inputted into a phase shift controller to update the phase shift angle β, for the purpose of regulating the heating power for temperature adjustment.

In the FM phase-locked loop module, to achieve zero-current conduction of NMOS, it is necessary to ensure that the rising edges of the drive pulses for Q1 and Q4 are aligned with the zero-crossing of the inverter current. Initially, square wave pulse voltages for Q1 drive and sinusoidal wave voltages from resonant capacitors are sampled and shaped through zero-crossing comparison. They are eventually converted into two square wave pulse signals with the same frequency but different phases. The MCU analyzes the phase difference between these two signals and adjusts the frequency through a phase-locked loop controller to achieve a phase difference of 90° between the two signals. This procedure eventually ensures zero-current conduction of NMOS.

In the temperature control process, the heating power is adjusted by the phase shift angle β change, which also will cause the variation of the phase difference between the Q1 drive pulse signal and the inner voltage of the resonant capacitor, and at this time, it is necessary to lock the phase difference by FM phase locking. Therefore, in the control system work, the temperature control module and the FM phase locking module can influence each other and must work in a coordination and balance state.

Figure 3(c) demonstrates the relative positions and dimensions of the inductor coil, heating tube, and temperature holding layer. The inductor heating coil has an inner diameter of 10 mm and a length of 32 mm, and the heating tube has an inner diameter of 5.6 mm and a length of 30 mm. The inductor

Preprints.org (www.preprints.org) | NOT PEER-REVIEWED | Posted: 31 July 2024 doi:10.20944/preprints202407.2474.v1

heating coil and the heating tube are filled with an aerogel temperature holding to minimize the thermal conduction from the heating tube to the inductor coil.

Figure 4 illustrates the driving principles of the full-bridge NMOS configuration. The four NMOSs are controlled by two half-bridge driver chips, with Q1 and Q2 forming one pair and Q3 and Q4 forming another pair. The input to the driver chips consists of two complementary pulse-width modulation (PWM) signals with a dead-time interval, generated by MCU PWM function. During system operation, when Q1 and Q4 are conducting while Q2 and Q3 are off, channel Q3 to Q2 are conducting and channel Q1 to Q4 are off. This alternation of conduction between these two diagonal NMOS pairs then can achieve inversion at terminals A and B. And when the two diagonal NMOS drive pulses are the same, the duty cycle of the U_{AB} voltage is 50%. When the drive pulses for these pairs are phase-shifted, the duty cycle of voltage U_{AB} decreases, along with its RMS value. The heating power then can be adjusted.

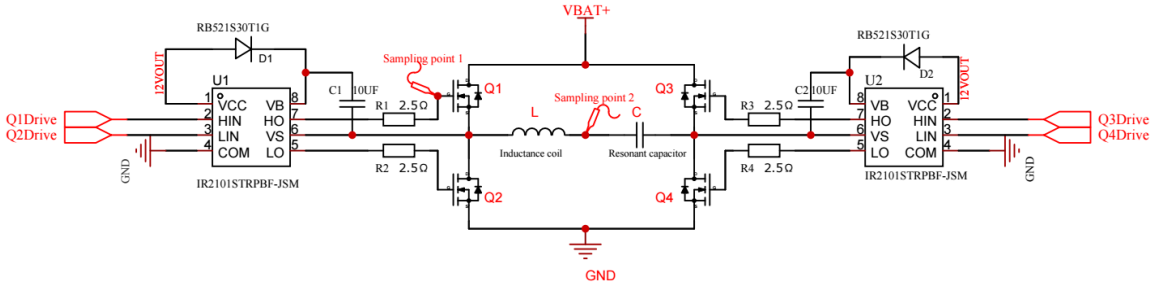

Figure 4. The circuit diagram of the full-bridge NMOS driver for the small-size electromagnetic induction heating control system powered by a 3.7V lithium battery.

Figure 5 shows the system FM phase-locked schematic diagram. The INA597 and LM311 are used to process the Q1 drive voltage and the voltage signal on the inside of the resonant capacitor. The INA597 is used to derate the signals to bring the voltage down to within the allowable range of the LM311 input voltage, and the LM311 compares the signals over zero and finally transforms the waveform into a 3.3v square wave voltage. Then two transformed pulse signals are input to the MCU for phase difference calculation, and according to which the frequency is then adjusted and locked. Finally, Q1,Q4 driving pulse is located at the zero crossing point of inverter current to realize the soft turn-on of NMOS.

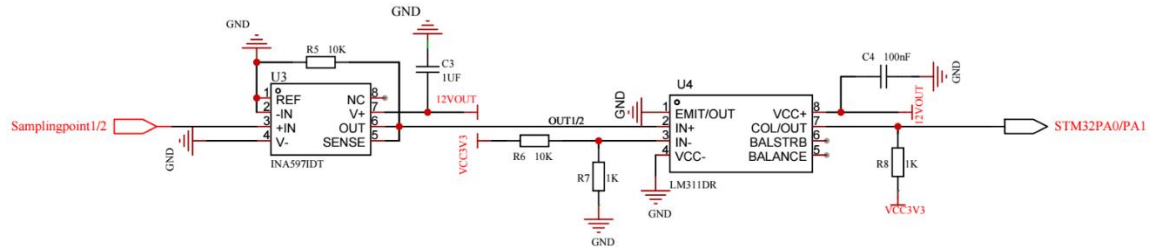

Figure 5. The frequency phase-locked circuit diagram for the Small-size Electromagnetic Induction Heating Control System powered by a 3.7V lithium battery.

2.3. Electromagnetic Induction Heating Control System Work Process

This system employs a combined phase-shifting and frequency-locking power adjustment method. By adjusting the duty cycle of the driving pulse signals for Q1~Q4 to increase the phase shift angle β, the value of U_{AB1} is changed. Simultaneously, the frequency-locking phase controller ensures that the rising edge of the driving pulse signals for Q1 and Q3 aligns with the zero-crossing point of the inverter circuit, thereby achieving soft switching. The STM32 timer can count cyclically between 0 and the auto-reload value (ARR). CCR is the value of the timer output comparison register. When the timer count value (INT) is greater than CCR, the timer outputs a low level, and vice versa outputs a high level. Therefore, the duty cycle of Q1,Q2 and Q3,Q4 can be adjusted by adjusting the value of

Preprints.org (www.preprints.org) | NOT PEER-REVIEWED | Posted: 31 July 2024 doi:10.20944/preprints202407.2474.v1

CCR, and Q1,Q2 and Q3,Q4 are complementary pulses with complementary duty cycles. The variable X is set within its range of 0~1, and the CCR is adjusted by the variable X. Its relationship with the CCR of the two sets of pulse signals is as follows

$$CCR1 = \frac{ARR * (1 + X)}{2} \tag{12}$$

$$CCR2 = \frac{ARR * (1 - X)}{2} \tag{13}$$

where CCR1 controls Q1,Q2 to drive the pulse duty cycle.CCR2 controls Q3,Q4 to drive the pulse duty cycle**.**

Figure 6 shows the driving pulses for Q1~Q4 during the system's power adjustment process, as well as some important waveforms. U_{AB} represents the square wave voltage on the inverter side, with an amplitude equal to the lithium battery's output voltage. When Q1 and Q4 are turned on while Q2 and Q3 are turned off, U_{AB} is positive. Conversely, when Q2 and Q3 are turned on while Q1 and Q4 are turned off, is negative. Thus, the inversion of voltage is achieved by controlling the on/off states of the diagonal pairs of NMOSs. The phase shift angle β is the interval angle between the driving pulses for Q1 and Q3. When the phase shift angle is β, the following applies:

$$U_{AB1} = \frac{2\sqrt{2}UDC}{\pi} \cdot \cos\frac{\beta}{2} \tag{14}$$

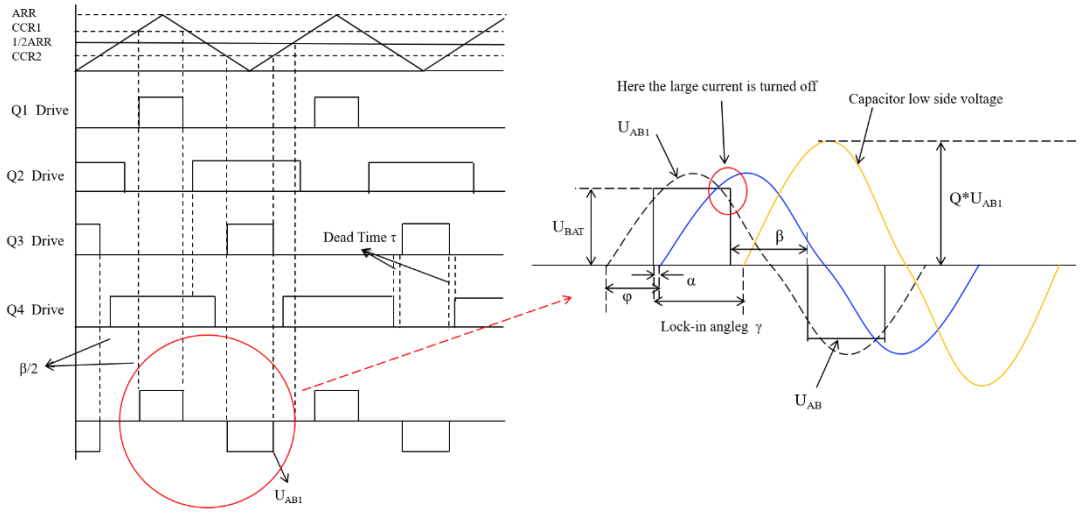

Figure 6. LC Series Resonant Circuit Operation Process and NMOS Drive Pulses and Related Important Waveforms during Power Adjustment Process.

When the phase shift is β, by adjusting the frequency, the zero-crossing point of I_{AB} is kept lagging behind the rising edge of the drive pulses for Q1 and Q3 by a very small phase shift angle α. The purpose of this adjustment is to provide sufficient time for the NMOS commutation and to approximately achieve zero-current switching. Considering that the voltage across the capacitor always lags the current I_{AB} by 90°in phase, this paper uses the voltage across the capacitor to phase-lock I_{AB}, with a phase-lock angle of 90°. By frequency modulation and phase-locking, Q1 and Q3 can be maintained in a soft turn-on and high current turn-off state during the power adjustment process, as shown in the right side of **Figure 6**.

Figure 7 describes the operation process of the heating non-combustion smoking device control system. It shows that the process can be divided into two periods: the heating and the temperature holding period. During the heating period, when the inverter frequency equals the resonant frequency, the duty cycle of the drive pulses for Q1 to Q4 is 50%, at which point X=0, β=0, U_{AB1} is at its maximum, and the inverter current is also at its maximum. This state is used to heat the heating element, rapidly raising its temperature to 250°C. At this time, all four NMOSs are in a soft-switching

 doi:10.20944/preprints202407.2474.v1

state, effectively avoiding large losses caused by high currents. When the system enters the temperature holding period, the value of X increases, the phase shift angle β increases, and the duty cycles of Q1 and Q3 decrease, while the duty cycles of Q2 and Q4 increase. With the frequency modulation and phase-locked control, the inverter frequency continuously increases from the resonant frequency, causing the duty cycle of the inverter voltage to drop from 50% to about 28%. During this process, the DC side current IDC gradually decreases until it stabilizes, and the temperature of the heating element ultimately stabilizes around 250°C. In the heating period, both the turn-on and turn-off of Q1 to Q4 are in a soft-switching state. In the temperature holding period, Q1 and Q3 are in a soft turn-on and high current turn-off state. The NMOS losses also change in different periods.

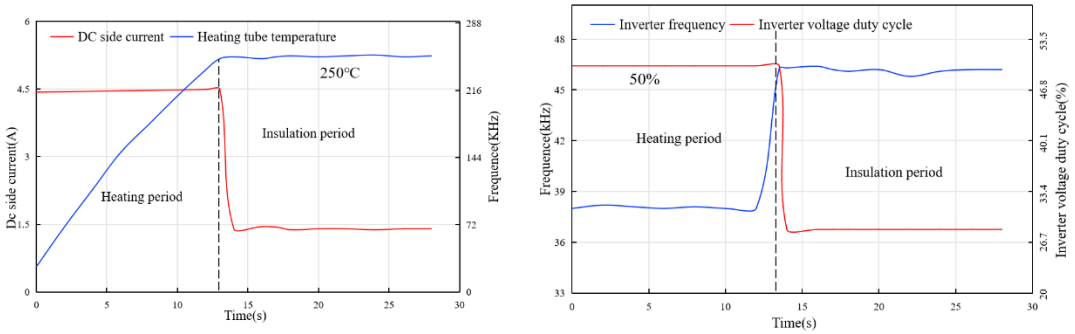

(**a**) (**b**)

Figure 7. Under the initial conditions of an inductor coil wire diameter of 1.17 mm, a resonant capacitor of 2.2 UF, and a heating tube with a 0.1 mm wall thickness made of pure iron, the variation of system parameters with operation time is shown. (**a**) The variation of the DC side current I_{DC} and the temperature of the heating tube over time. (**b**) The variation of the inverter frequency f and the inverter voltage duty cycle D with time.

2.4. Impact Factors Analysis of NMOS Losses

The total loss of NMOS in the small electromagnetic induction heating control system mainly consists of three parts: the conduction loss and driving loss of all NMOSs in the heating and temperature holding period, and the turn-off loss of NMOS Q1, Q3 in the temperature holding period. In order to optimize the NMOS loss, the above three losses are calculated and influencing factors are analyzed.

In the full-bridge LC series resonant circuit structure of **Figure 2(a)**, the output power on the DC side is approximately equal to the output power on the inverter side, so the following equation can be obtained:

$$U_{DC} \cdot I_{DC} = U_{AB1} \cdot I_{AB} \cdot \cos\varphi \tag{15}$$

The inverter current is:

$$I_{AB} = \frac{U_{DC} \cdot I_{DC}}{U_{AB1} \cdot \cos\varphi} \tag{16}$$

where:

$$\varphi = \frac{\beta}{2} \tag{17}$$

From the waveform relationship in **Figure 8**, we obtain:

$$\frac{1}{2\pi} = \frac{D}{\pi - \beta} \tag{18}$$

$$\frac{\beta}{2} = \frac{\pi}{2}(1 - 2D) \tag{19}$$

Preprints.org (www.preprints.org) | NOT PEER-REVIEWED | Posted: 31 July 2024 doi:10.20944/preprints202407.2474.v1

where β is the phase shift angle and D is the duty cycle of the drive pulses for Q1 and Q3.

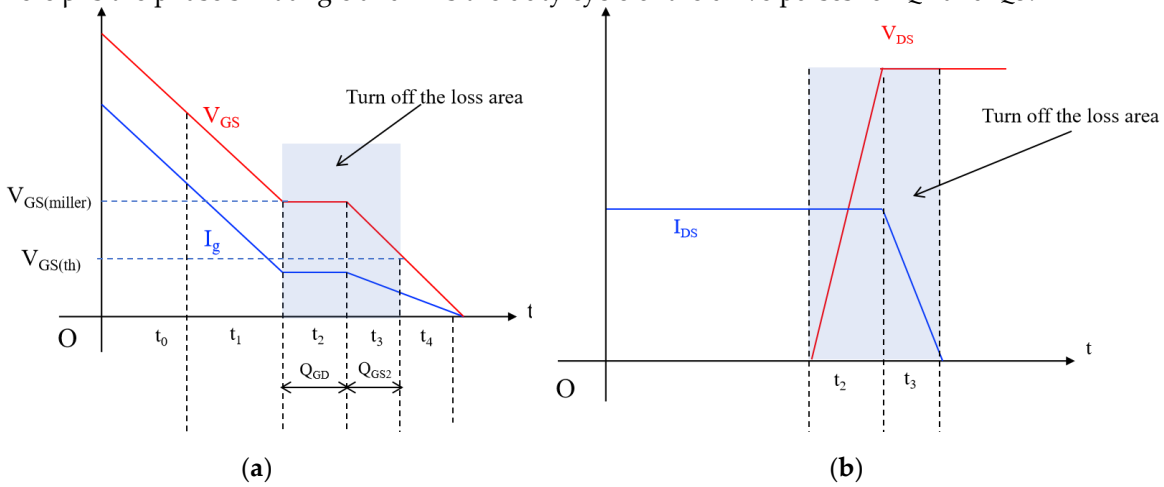

Figure 8. Figure showing the turn-off process of Q1. (**a**) The changes in the gate-to-source voltage V_{GS} and gate drive current Ig during the turn-off process of Q1. (**b**) The variations in the drain-to-source voltage V_{DS} and drain current I_{DS} with time during the turn-off process of Q1.

Substituting into Equation (13):

$$I_{AB} = \frac{I_{DC} \cdot \pi}{2\sqrt{2} \cdot \left[\cos\frac{\pi}{2}(1-2D)\right]^2} \tag{20}$$

At this time, the off-state current in the circuit is:

$$I_{off} = I_{AB} \cdot \sqrt{2} \cdot \sin\theta \tag{21}$$

where θ is the angle corresponding to the high level of the Q1 pulse.

From the circuit state relationship:

$$\frac{1}{2\pi} = \frac{D}{\theta} \tag{22}$$

$$\theta = 2 \cdot \pi \cdot D$$

Substitute into Equation (20):

$$I_{off} = \frac{\pi \cdot I_{DC} \cdot \sin 2\pi D}{2 \cdot \left[\cos\frac{\pi}{2}(1-2D)\right]^2} \tag{23}$$

From the analysis of the **Figure 8,** it can be seen that the switching states of the diagonally opposite switches directly determine the direction and duty cycle of the inverter-side output voltage. Therefore, the diagonally opposite switches are grouped into pairs: Q1 and Q4 form one group, while Q2 and Q3 form another group. Since these two groups are symmetrical, only the loss analysis of Q1 and Q4 is required, where Q1 is the upper bridge arm and Q4 is the lower bridge arm.

The conduction loss calculation formula for Q1 and Q4 is approximately:

$$P_{Q1CON} = {I_{AB}}^2 \cdot R_{DS(ON)} \cdot D \tag{24}$$

$$P_{Q4CON} = {I_{AB}}^2 \cdot R_{DS(ON)} \cdot [D + (1+2D)/2] \tag{25}$$

Substitute I_{AB} from Equation (14) to obtain:

$$P_{Q1CON} = \frac{{I_{DC}}^2 \cdot \pi^2}{8 \cdot \left[\cos\frac{\pi}{2}(1-2D)\right]^4} \cdot R_{DS(ON)} \cdot D \tag{26}$$

 doi:10.20944/preprints202407.2474.v1

$$P_{Q4CON} = \frac{{I_{DC}}^2 \cdot \pi^2}{8 \cdot \left[\cos\frac{\pi}{2}(1-2D)\right]^4} \cdot R_{DS(ON)} \cdot [D + (1+2D)/2] \tag{27}$$

where D is the duty cycle of the Q1 driving pulse. During the heating period, D=0.5, at which time：

$$P_{Q1CON} = P_{Q4CON} \tag{28}$$

The calculation formula for the driving loss of Q1 and Q4:

$$P_{Q1DRV} = P_{Q4DRV} = V_{DRV} \cdot f \cdot Q_g \tag{29}$$

where V_{DR} is the NMOS's driving voltage, f is the inverter-side frequency, and Q_g is the total gate charge of the NMOS. During the heating and temperature holding periods, the driving losses of Q1 and Q4 are the same.

From the above analysis, during the heating period, there are no turn-off losses for Q1 and Q4, while during the temperature holding period, only Q1 introduces turn-off losses. **Figure 8** shows the variation of parameters during the turn-off process. V_{DS} is the NMOS drain-source voltage, I_{DS} is the NMOS drain-source current, V_{GS} is the NMOS gate-source voltage, V_{BAT} is the battery supply voltage, and I_g is the NMOS gate drive current.

It is observed that the turn-off process mainly consists of two stages: t_2 and t_3. In stage t_2, I_{DS} remains constant, and V_{DS} rises rapidly to the V_{BAT}. During this stage, the V_{DS} and gate driving current remain unchanged, and the V_{DS} is at the Miller plateau(A time period in which V_{GS} is held constant and the V_{DS} voltage gradually rises or falls under the action of I_g); the charge discharged in this stage is denoted as Q_{GD}. In stage t_3, the V_{DS} remains constant while the current drops quickly to zero. During this stage, the V_{DS} drops to $V_{GS(th)}$, and the gate driving current decreases; the charge discharged in this stage is denoted as Q_{GS2}.

Based on the geometric relationship in **Figure 8(b)**, the Q1 turn-off loss during this stage is approximately:

$$P_{Q1OFF} = \frac{1}{2} \cdot f \cdot U_{off} \cdot I_{off} \cdot t_{off} \tag{30}$$

where f is the inverter-side frequency, U_{off} is the turn-off voltage, which is equal to the lithium battery supply voltage. I_{off} is the turn-off current, which is calculated using Equation (21). t_{off} is the turn-off loss time, consisting of two parts: t_2 and t_3. where

$$t_2 = \frac{Q_{GD}}{I_{g1}} \tag{31}$$

$$I_{g1} = \frac{V_{GS(miller)}}{R_g} \tag{32}$$

$$t_3 = \frac{Q_{GS2}}{I_{g2}} \tag{33}$$

$$I_{g2} = \frac{\frac{1}{2}\left(V_{GS(miller)} + V_{GS(th)}\right)}{R_g} \tag{34}$$

$$t_{off} = t_2 + t_3 \tag{35}$$

The total loss of Q1,Q4 during the heating period is

$$P_{Q1\ heating\ loss} = P_{Q1CON} + P_{Q1DRV} \tag{36}$$

$$P_{Q4\ heating\ loss} = P_{Q4CON} + P_{Q4DRV} \tag{37}$$

Preprints.org (www.preprints.org) | NOT PEER-REVIEWED | Posted: 31 July 2024 doi:10.20944/preprints202407.2474.v1

And at this time Q1,Q2,Q3,Q4 have the same loss of power

$$P_{Q1\ \text{heating loss}} = P_{Q2\ \text{heating loss}} = P_{Q3\ \text{heating loss}} = P_{Q4\ \text{heating loss}} \quad (38)$$

During the holding time, the total loss of Q1,Q4 is

$$P_{Q1\ \text{temperature holding loss}} = P_{Q1CON} + P_{Q1DRV} + P_{Q1OFF} \quad (39)$$

$$P_{Q1\ \text{temperature holding loss}} = P_{Q4CON} + P_{Q4DRV} \quad (40)$$

At this time, the losses of the upper bridge arm NMOS Q1,Q3 are the same, and the losses of Q2 and Q4 are the same.

$$P_{Q1\ \text{temperature holding loss}} = P_{Q3\ \text{temperature holding loss}} \quad (41)$$

$$P_{Q4\ \text{temperature holding loss}} = P_{Q2\ \text{temperature holding loss}} \quad (42)$$

Figure 9(a) shows the trend of Q1's conduction loss with varying inverter-side duty cycle under different DC-side currents I_{DC} and its own on-resistance $R_{DS(on)}$. It is clear that the conduction loss decreases with the increase of the inverter voltage duty cycle, regardless of the conditions. Additionally, for a constant $R_{DS(on)}$, the loss increases with increasing I_{DC}. For a constant I_{DC}, the loss increases with increasing $R_{DS(on)}$, and Q4 exhibits the same variation pattern as Q1.

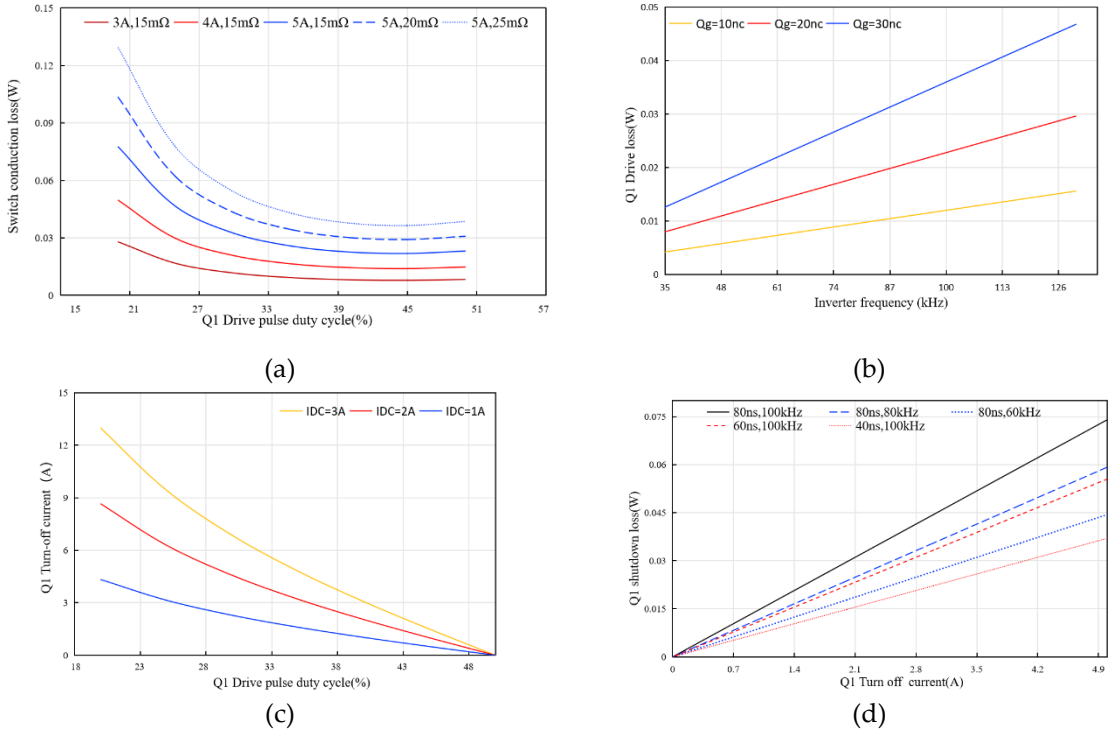

Figure 9. Analysis of Various Loss Factors for NMOSs Q1 and Q4. (**a**) The conduction loss of Q1 varies with the duty cycle of its driving voltage for different I_{DC} and $R_{DS(on)}$. (**b**) The trend of the NMOS's driving loss with increasing inverter frequency f under different gate total charges Q_g. (**c**) The variation of Q1's turn-off current with the driving voltage duty cycle for different I_{DC}. (**d**) Q1's turn-off loss changes with the turn-off current under different t_{off} and f.

Figure 9(b) illustrates the trend of the driving loss of the NMOS with increasing inverter frequency f under different gate total charges Q_g. It is found that its loss increases with increase in inverter frequency and increases with increase in its own Q_g.

Figure 9(c) shows the trend of Q1's turn-off current as the inverter-side duty cycle changes under different DC-side currents I_{DC}. It shows that for the same IDC, the higher the duty cycle, the lower the shutdown current. At the same duty cycle, a larger I_{DC} corresponds to a larger turn-off current.

 doi:10.20944/preprints202407.2474.v1

Figure 9(d) demonstrates the trend of Q1's turn-off loss with varying turn-off current under different turn-off times t_{off} and inverter frequencies f. It can be seen that the turn-off loss increases as the turn-off current increases in any case. Furthermore, for a constant t_{off}, the loss increases with increasing f. For a constant f, the turn-off loss increases with increasing t_{off}.

The above analysis reveals that the conduction loss of the NMOS is mainly related to its own on-resistance $R_{DS(on)}$, the DC-side current I_{DC}, and the inverter-side duty cycle D. The driving loss is primarily influenced by the inverter frequency f, the NMOS's own parameters Q_g, and the driving voltage V_{DRV}. The turn-off loss is mainly associated with the turn-off time t_{off}, the turn-off current I_{off}, and the inverter frequency f, where the turn-off current is primarily determined by the DC-side current I_{DC} and the inverter-side duty cycle D.

2.5. Experiment Setup

To improve the performance of the control system, the influence of circuit parameters including resonant capacitance value, the wire diameter of the induction heating coil, the material and wall thickness of the heating tube on the performance of the heating system was studied through experiments.

Experiments were conducted using a 1.17mm induction coil wire diameter to explore the impact of capacitance changes on the heating rate of the tube and to calculate the NMOS total loss value at each stage simultaneously for the control system's performance. To investigate the effect of different induction coil wire diameter, experimental tests are carried out on coils with five wire diameters of 1.17, 1.32, 1.5, 1.65 and 1.75 mm. The heating rate of the heating tube is recorded at different capacitance values, and the NMOS total loss value are calculated at each stage. Three commonly used representative materials in induction heating, Iron, 430 stainless steel, and 1J50 soft magnetic alloy, were selected for experimentation. **Table 1** shows the physical parameters of the three materials. At the same time, in order to investigate the effect of wall thickness on the performance of the control system, heating tubes with different wall thicknesses of 0.1, 0.2, 0.3, and 0.4 mm were employed to investigate the effect of wall thickness on the heating rate and the NMOS total loss.

Table 1. Comparison of Physical Properties of Three Commonly Used Materials for Induction Heating.

Material	Density(g/cm³)	Relative permeability	Thermal conductivity(w/m·℃)	Specific heat capacity(J/kg·℃)
Pure iron	7.86	4000	46.5	460
430 stainless steel	7.75	500	23.9	460
1j50 soft magnetic alloy	8.2	20000	16.5	450

Figure 10(a) displays the experimental setup for evaluating the performance of a small electromagnetic induction heating control system. A regulated power supply replaces a 3.7V lithium battery to enable easier monitoring of output current. Program commands were sent from PC to the control system MCU and monitors the frequency and duty cycle of the oscilloscope's output waveforms during the experiment. An infrared temperature meter measures the actual temperature rise of the NMOS. **Figures 10(c), (d), and (e)** compare the appearance of materials used, the wire diameter of the induction heating coil, and the wall thickness of the heating tube, respectively. **Figure 10(f)** illustrates the method used to measure the heating rate of the tube: an infrared temperature measuring instrument observes the temperature distribution, revealing a ladder-like pattern with the highest temperature in the middle. To precisely control this peak temperature, a K-type thermocouple is positioned at the center of the heating tube. A small opening is cut in the middle of the induction heating coil to guide the thermocouple, preventing temperature drift caused by the coil's high-frequency magnetic

Preprints.org (www.preprints.org) | NOT PEER-REVIEWED | Posted: 31 July 2024 doi:10.20944/preprints202407.2474.v1

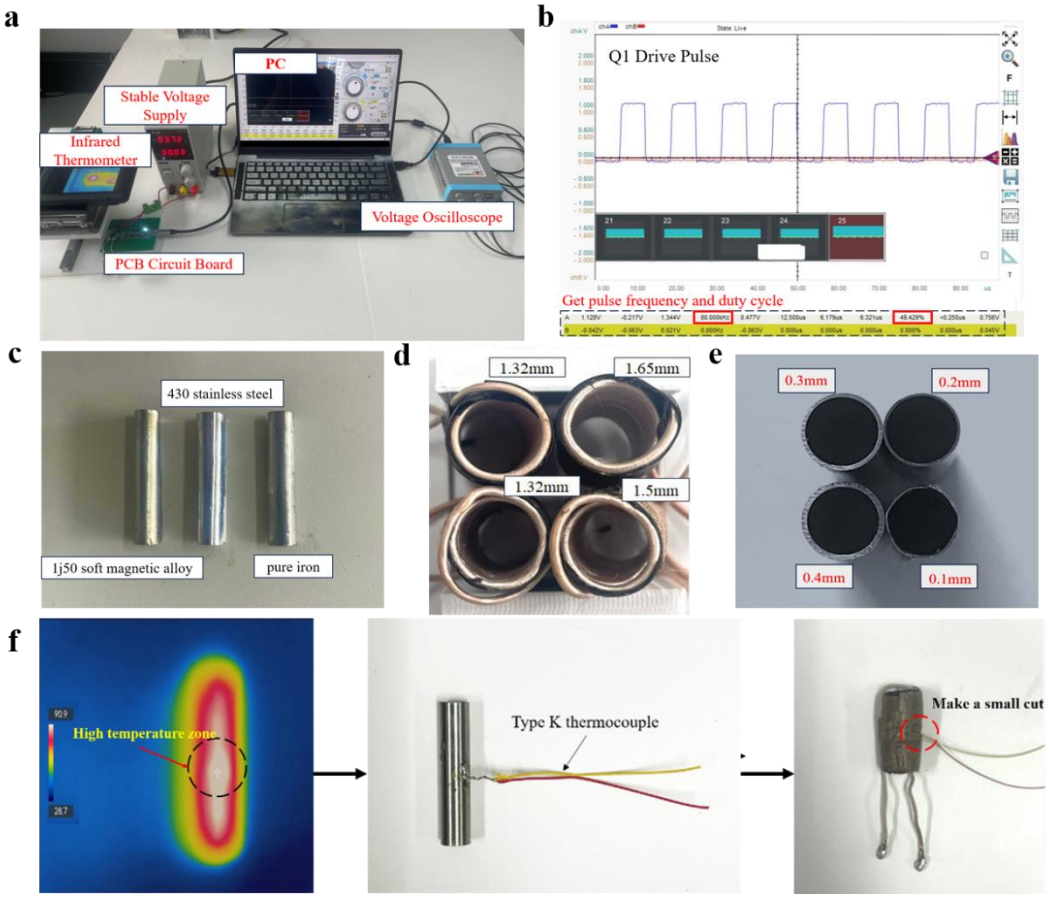

Figure 10. Experimental setup (**a**) The experimental platform for performance testing of a small induction heating control system. (**b**) The output waveforms from the oscilloscope. (**c**) Three experimental materials: iron, 430 stainless steel, and 1j50 iron-nickel soft magnetic alloy. (**d**) Induction coil wire with different diameters. (**e**) The appearance of different wall thicknesses of heating tubes. (**f**) The temperature distribution of the heating tube and the arrangement of type K thermocouples.

3. Results and Discussion

Correct NMOS parameter selection is crucial as turn-off losses can significantly outweigh other losses. Therefore, minimizing turn-off losses is prioritised in NMOS selection, followed by reducing other losses. This paper employs the NCEP3065QU NMOS model (Wuxi New Clean Energy, China) as the inverter's switching tube. Table 2 details the parameters for this NMOS model, showing a total of approximately 8 nC for Q_{GD} and Q_{GS2} at a 12V gate drive voltage, Q_g around 30 nC, and an $R_{DS(on)}$ of just 1.9 mΩ.

Table 2. N-channel MOS tube NCEP3065QU parameter details.

Model	Qg(nc)	$R_{DS(on)}$(mΩ)	Q_{GD}(nc)	Q_{GS2}(nc)	t_{off}(ns)
NCEP3065QU	About 30	1.9	about 5	about 3	About 25

3.1. Effect of Resonant Capacitance Value on Heating Rate and NMOS Loss

A pure ferrous heating tube with a 0.1 mm wall thickness and 1.17 mm coil wire diameter were used to examine the effect of capacitance on the operating performance of the control system. **Figure 11(a)** illustrates the impact of increasing capacitance on the DC side current and inverter frequency of the system during both heating and temperature holding periods. **Figure 11(b)** depicts the variation in the heating rate of the heating tube and the power losses of Q1 and Q4 during these periods as capacitance increases (Q2 and Q3 show symmetrical losses). It shows that as the frequency decreases, both Q1 and Q4 exhibit a reduction in losses during the holding period. However, due to

 doi:10.20944/preprints202407.2474.v1

increased current during heating, losses slightly increase in this phase. Since the temperature holding period is significantly longer than the heating period, losses during holding play a major role in the NMOS temperature rise. Therefore, increasing capacitance overall helps reduce NMOS temperature rise losses. Additionally, increasing capacitance initially enhances the heating rate of the heating tube. However, once capacitance exceeds a certain value, further increases lead to diminishing returns in heating rate enhancement.

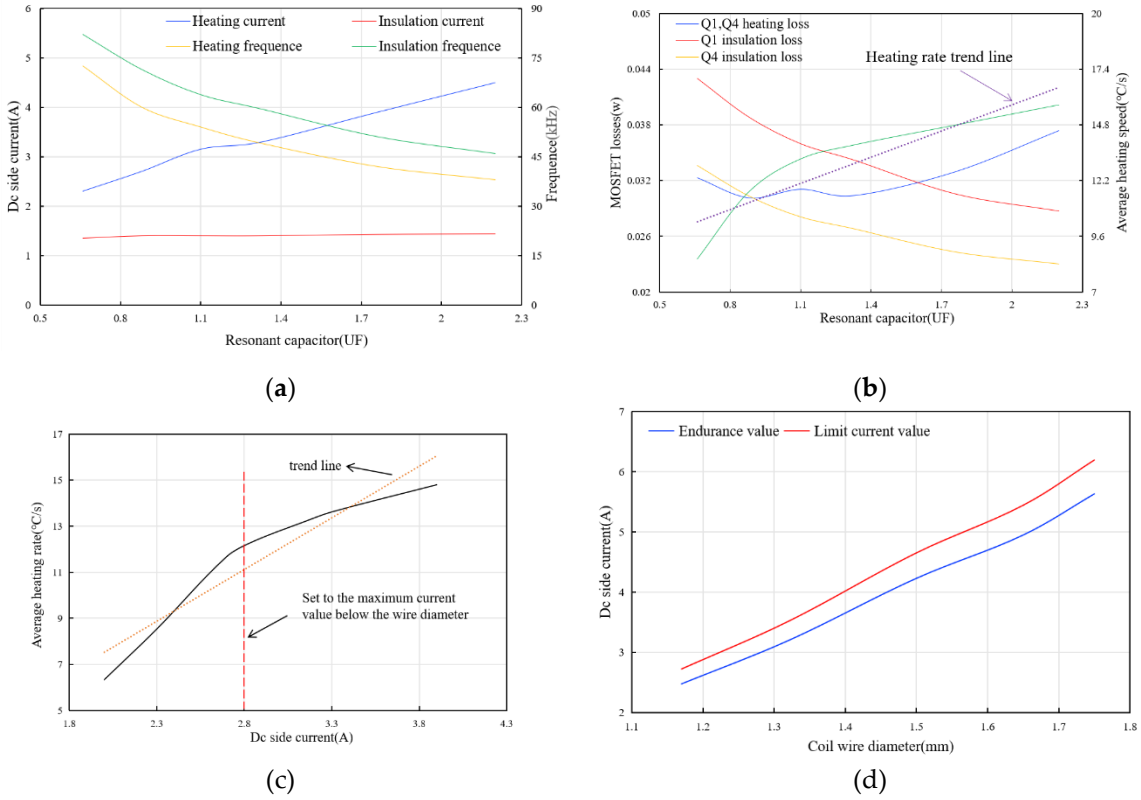

Figure 11. Experimental results under initial circuit conditions with a coil wire diameter of 1.17 mm and a 0.1 mm Thick pure iron heating tube. (**a**) DC-side current IDC and inverter frequency f during the heating and temperature holding periods as the capacitance increases. (**b**) NMOSs Q1 and Q4 losses and the heating rate of the heating tube during the heating and temperature holding periods as the capacitance increases. (**c**) Trend of the average heating rate of the heater with increasing DC side current. (**d**) Current withstand and limit values of coils correspond to the DC side current in relation to the coil wire diameter.

Figure 11(c) shows the relationship between the time required for the heating tube to reach 250°C and the corresponding average heating rate as the DC measured current increases. The average heating rate is given by:

$$\frac{250℃(\text{target temperature})-27℃(\text{room temperature})}{\text{heating time}} \quad (43)$$

It shows that the heating rate of the heating tube increases as the current increases. However, when the inverter current exceeds 1.1 times the maximum current rating of the coil wire diameter, the increase in the heating rate of the heating tube significantly slows down. Therefore, this paper defines 1.1 times the current rating of the wire diameter as the maximum current value for that wire diameter.

This study initially experimented with a 1.17mm coil wire diameter and a 0.1mm wall thickness iron tube heating tube to investigate the impact of capacitance on circuit parameters. It was observed that increasing the capacitance of the resonant capacitor enhances the heating rate to a certain extent and effectively reduces NMOS tube losses during heat preservation. However, excessive capacitance can decrease battery efficiency, as shown in **Figure 11(a)**, where exceeding 0.88 μF leads to current surpassing the coil wire diameter's limit, causing rapid resistance and temperature rise, and diminishing battery efficiency. Therefore, selecting an appropriate capacitance value that ensures

 doi:10.20944/preprints202407.2474.v1

current within the wire diameter's limit improves NMOS efficiency, heating rate, and battery efficiency. **Figure 11(d)** illustrates the relationship between DC side current, current withstand value, limit current, and coil wire diameter.

3.2. Effect of Induction Coil Wire Diameter on Heating Rate and NMOS Loss

Figures 12(a), **(b)**, and **(c)** illustrate NMOS losses (Q1 and Q4) during heating and temperature holding periods, and the heating tube's rate, across different wire diameters (0.1 mm wall thickness) for pure iron, 1J50 soft magnetic alloy, and 430 stainless steel. During heating, Q1 and Q4 losses increase consistently. In the holding period, losses for pure iron initially decrease then rise, while remaining stable for the other materials until wire diameters exceed 1.4 mm, where they gradually increase. Increasing wire diameter enhances heating rates, but beyond 1.5 mm, the rate slows, likely due to nearing magnetic saturation. This diameter corresponds to a battery output of approximately 4.5 A; larger diameters decrease battery efficiency and increase NMOS losses. To ensure fair performance comparison at constant battery output, a 1.5 mm wire diameter is used for the induction coil.

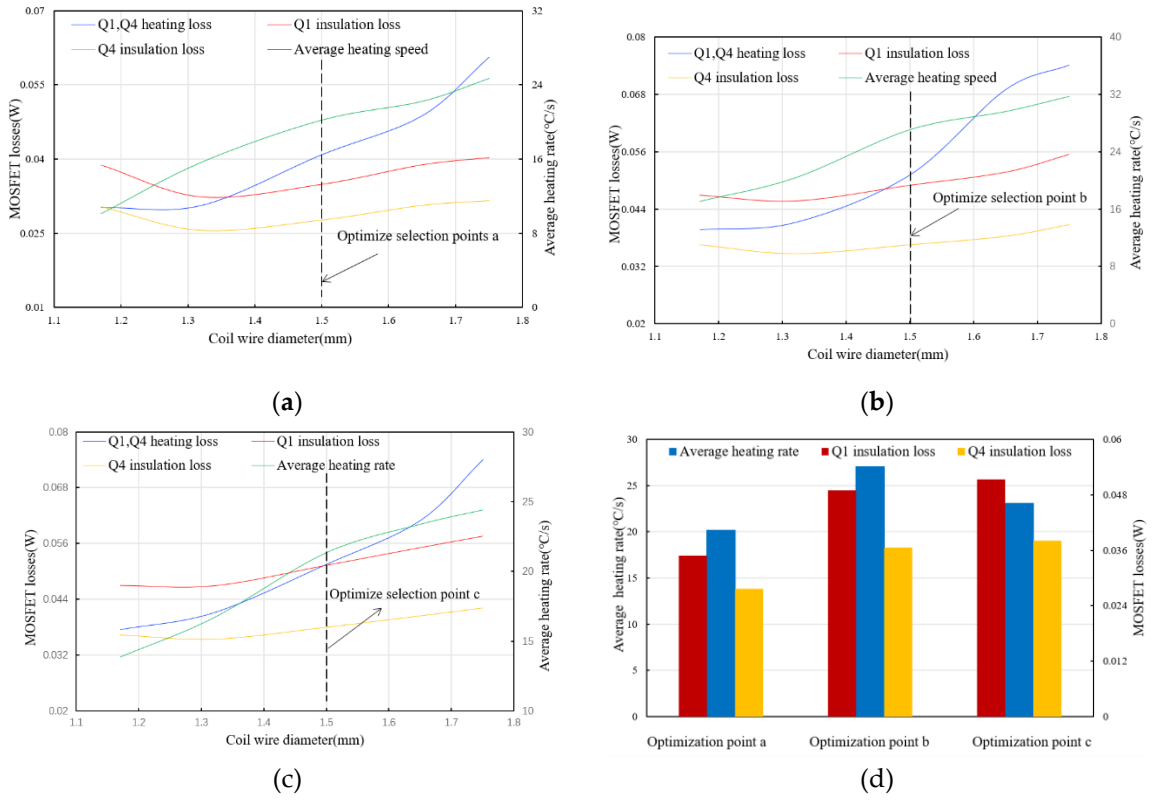

Figure 12. Effects of wire diameter on NMOS losses and heating rates in induction heating systems (a) Losses of Q1 and Q 4 and heating rate variation with wire diameter for pure iron heating tube (0.1 mm wall thickness). (b) Losses of Q 1 and Q 4 and heating rate variation with wire diameter for 1j50 soft magnetic alloy heating tube (0.1 mm wall thickness). (c) Losses of Q 1 and Q 4 and heating rate variation with wire diameter for 430 stainless steel heating tube (0.1 mm wall thickness). (d) Comparison of heating rate and losses of Q 1 and Q 4 at optimized conditions (points a, b, c).

Therefore, this paper selects a 1.5mm induction heating wire diameter under 0.1mm wall thickness for pure iron, 1J50 soft magnetic alloy, and 430 stainless steel heating tubes. Capacitance values are adjusted to set the battery output current to 4.6 A, optimizing circuit conditions at points labeled a, b, and c. **Figure 11(d)** compares heating tube rates and Q1, Q4 losses during holding periods at these points. Analysis shows points b and c achieve significantly faster heating rates than point a, despite higher losses during holding. Specifically, with constant battery output power, 1J50 soft magnetic alloy and 430 stainless steel heat faster but also experience greater NMOS losses.

 doi:10.20944/preprints202407.2474.v1

3.3. Effect of Heating Tube Wall Thickness on Heating Rate and NMOS Loss

Figure 13(a), **(b)**, and **(c)** respectively show the variation in heating rate with increasing wall thickness for heating tubes made of pure iron, 1J50 soft magnetic alloy, and 430 stainless steel, along with the corresponding NMOS losses (Q1 and Q4) during the heating and temperature holding periods, under conditions of 1.5 mm wire diameter and 4.6 A battery output current. It was observed that all three materials exhibited a noticeable decrease in heating tube heating rate with increasing wall thickness, with slight reductions in Q1 and Q4 losses during the heating and temperature holding periods.

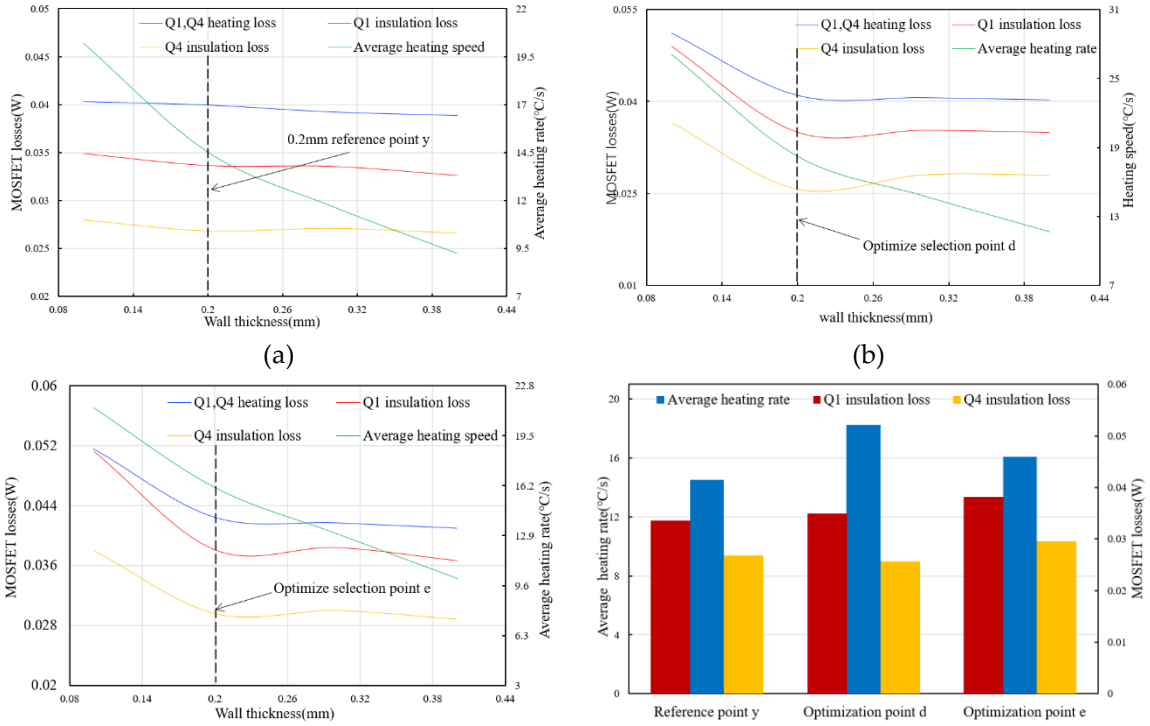

Figure 13. Impact of wall thickness on NMOS losses and heating rates in induction heating systems **(a)** Changes in Q 1 and Q 4 losses and heating rate with increasing wall thickness for pure iron heating tube. **(b)** Changes in Q 1 and Q 4 losses and heating rate with increasing wall thickness for 1j50 soft magnetic alloy heating tube. **(c)** Changes in Q 1 and Q 4 losses and heating rate with increasing wall thickness for 430 stainless steel heating tube. **(d)** Comparison of heating rate and Q 1, Q 4 losses during holding period at optimization points e, f, and g.

For iron heating tubes, Q1 and Q4 losses show minimal change with increased wall thickness. Therefore, a 0.1 mm wall thickness remains optimal for pure iron heating tubes due to faster heating rates. In contrast, 1J50 soft magnetic alloy and 430 stainless steel behave differently. When their wall thickness increases to 0.2 mm, Q1 and Q4 losses notably decrease, especially for 1J50 soft magnetic alloy. This is because at 0.1 mm thickness, both materials experience a continuous increase in battery output current during heating, akin to nearing no-load conditions. Increasing the circuit's inversion frequency to limit current results in significantly higher NMOS losses compared to pure iron. A 0.2 mm wall thickness reduces this no-load effect. As thickness further increases, losses for these materials stabilize. Therefore, while the heating rate for 1J50 soft magnetic alloy and 430 stainless steel with 0.2 mm thickness may not match that of 0.1 mm, NMOS losses in the system are markedly improved.

Therefore, in this paper, under the 0.2mm wall thickness of 1j50 soft magnetic alloy and 430 stainless steel heating tube material, the induction coil wire diameter are selected 1.5mm, and at the same time, the capacitance value is adjusted so that the output current of the battery reaches 4.6A, so as to optimize the circuit conditions of point d and point e. Meanwhile, in order to compare the

 doi:10.20944/preprints202407.2474.v1

performance of the control system under the three materials with 0.2mm wall thickness, this paper also adjusts the output current of the battery to 4.6A under the 0.2mm wall thickness of the pure iron heating tube, and optimizes the reference point y. **Figure13(d)** demonstrates the heating rate of the heating tube under the optimized points y, d, and e, as well as the trend of the loss of Q1, Q4 in the temperature holding period with the increase of wall thickness. By analyzing this figure, it is found that under 0.2 mm wall thickness, the heating rate at points d and e is slowed down, but the loss is significantly reduced, especially at point d, which is approximately the same as that under the condition of the same wall thickness of ferrous heating tube.

3.4. Comparison and Analysis of the Initial Selection Point and Optimization Points

Under consistent battery output current, the heating rate of the heating tube and the NMOS losses during both heating and holding periods are measured as benchmarks. Through comparison and analysis, five optimization points are selected. At these points, the control system's induction coil wire diameter is set to 1.5mm, with the battery current fixed at 4.6A. To compare the control system's performance with the initial setup using a 1.17mm wire diameter and 0.1mm wall thickness iron heating tube, adjustments are made to the heating tube material, wall thickness, and circuit resonant capacitance. This paper identifies these adjustments as optimization point x. **Table 3** details specific circuit parameters across the five optimization points (a, b, c, d, e, x).

Table 3. Comparison of circuit conditions for 6 optimization selection points.

Selection point	Material	Coil wire diameter (mm)	Wall thickness (mm)	Capacitance value(UF)	Average heating power(w)
Optimal Point x	Pure iron	1.17	0.1	2.2	about 17
Optimal point a	Pure iron	1.5	0.1	2.3	about 17
Optimal point b	Soft magnetic alloy	1.5	0.1	0.86	about 17
Optimal point c	430 stainless steel	1.5	0.1	0.96	about 17
Optimal point d	Soft magnetic alloy	1.5	0.2	1.95	about 17
Optimal point e	430 stainless steel	1.5	0.2	1.75	about 17

Figure 14(a) compares NMOS loss values at 6 selected points. **Figure 14(b)** contrasts the heating time required for the heating tubes and the temperature rise of NMOSs after 5 minutes of system operation at these points. Result reveals that temperature rise at each point correlates closely with calculated loss values. Throughout, Q1 shows higher temperature rise than Q4. Points b and c exhibit notably higher NMOS temperature rises, with Q1 exceeding 75°C at point c. Point e falls in the middle, while points a and d show similar, relatively low temperature rises. Point x shows the smallest temperature rise. Regarding heating time, point b requires the shortest duration, followed by points c, a, and d, while points x and e require the longest. It can be seen that points b and c have very fast heating rates, but at the same time introduce a large NMOS temperature rise to the system, and point X has a small NMOS temperature rise, but due to the coil's own loss, its battery efficiency is low and the heating time is long. Only point a has good performance in both heating rate as well as NMOS temperature rise at the same time. Therefore, to improve the comprehensive performance of the control system, point a is selected as the best optimization point of this system, which has a faster heating rate and relatively small loss.

Preprints.org (www.preprints.org) | NOT PEER-REVIEWED | Posted: 31 July 2024 doi:10.20944/preprints202407.2474.v1

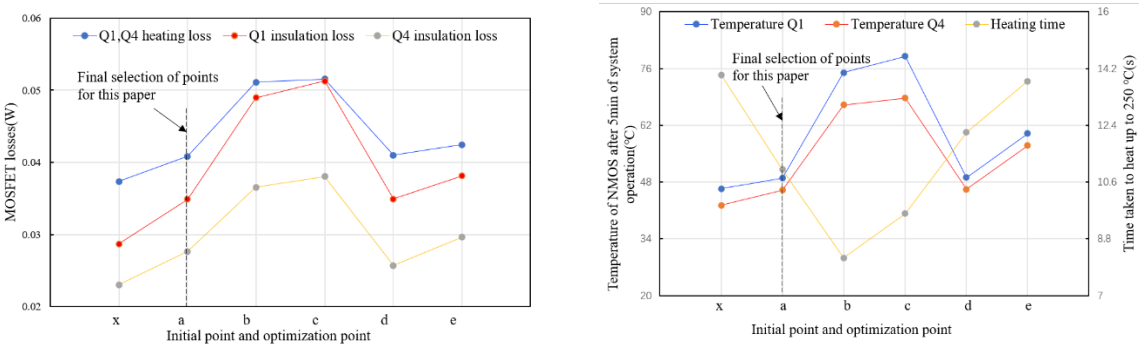

(a) (b)

Figure 14. Performance analysis of NMOS losses and heating dynamics in induction heating systems (**a**) NMOS loss values (Q1, Q4) during heating and temperature holding at 6 optimization points. (**b**) Heating time and NMOS temperature rise (Q1, Q4) after 5 minutes of operation at 6 optimization points.

Figure 15(a) shows the infrared temperature distribution images of the NMOS after running the device for 1 min, 2 min, 3 min, 4 min, and 5 min, respectively, under the circuit conditions of the optimization point a finally selected. **Figure15(b)** depicts the 3D thermographic images of the four NMOSs after running the device for 5 min under the circuit condition of optimization point a. By analyzing this figure, there is no significant difference in the temperature rise of the four NMOS during the heating time period, but with the growth of the device operation time, the overall temperature rise of Q1,Q3 starts to be larger than that of Q2,Q4, and the temperature rise of Q2,Q4 is basically the same, and Q1,Q3 is slightly different due to the error of component parameters. **Table 4** records in detail the performance of the control system operating performance under the circuit conditions at point a. Under the battery output current of 4.6A, the temperature of the upper bridge arm Q1,Q3 is 49℃ and 49.8℃, the temperature of the lower bridge arm Q2,Q4 is about 46℃, and the temperature of the outer layer of the coil is about 60℃ during the device running time of 5min.

Table 4. Optimal control system performance parameters.

Optimal point	Battery output current(A)	Heating time(s)	Q1 final temperature (℃)	Q3 final temperature (℃)	Q2,Q4 final temperature (℃)	Coil outer temperature (℃)
a	4.6A	11	49	49.8	About 46	About 60

 doi:10.20944/preprints202407.2474.v1

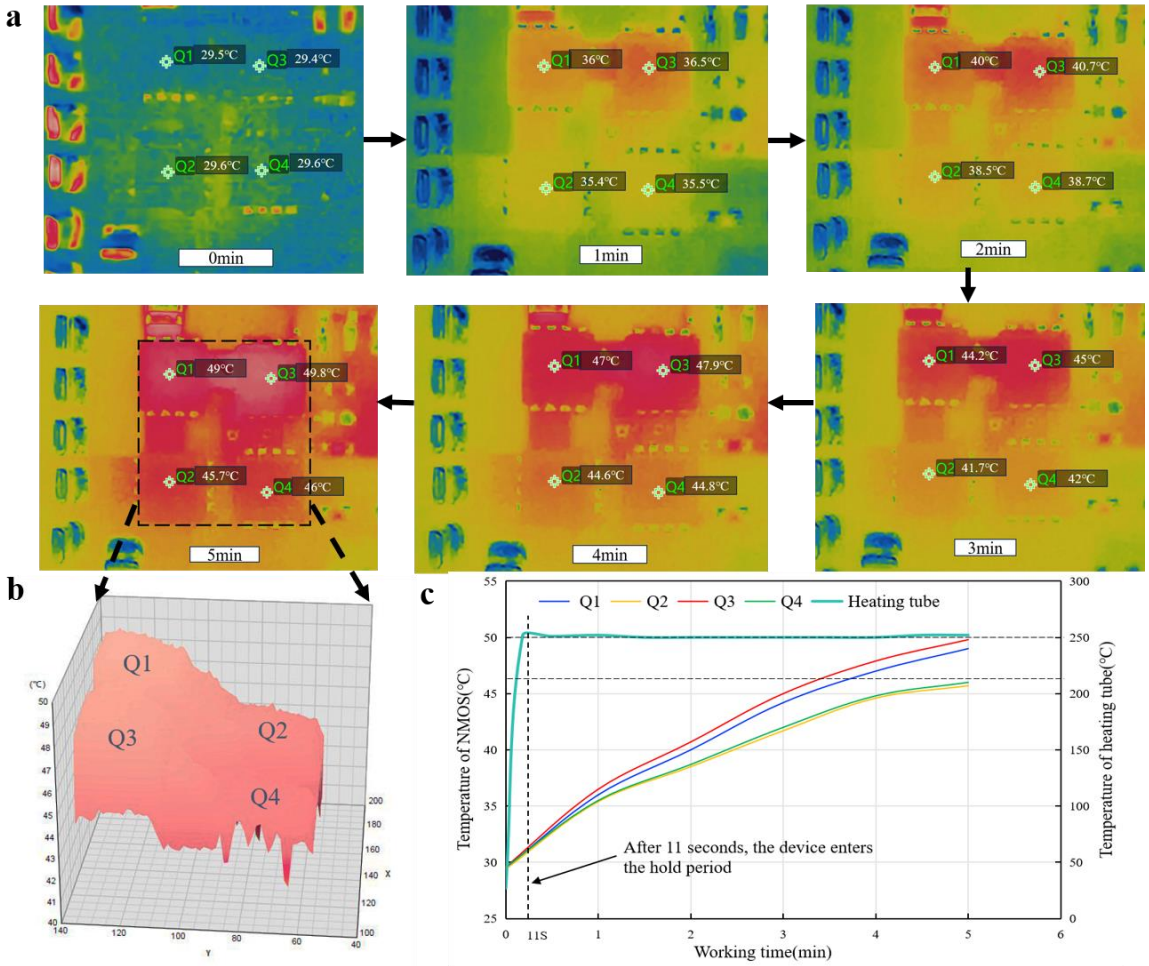

Figure 15. Thermal analysis of NMOS and heating tube in induction heating system (**a**) Infrared temperature distribution of NMOS after running the device for 1 min, 2 min, 3 min, 4 min and 5 min, respectively. (**b**) 3D thermogram of NMOS after running the device for 5 min.(**c**) Trend of NMOS as well as heating tube temperature with device running time.

4. Conclusions

This paper presents a small size electromagnetic induction heating control system based on a full-bridge LC series resonant circuit powered by a 3.7V lithium battery. By adjusting the resonant capacitor value, the system achieves load impedance matching. The paper focuses on design and optimization experiments for the application of this system in heating non-combustible smoking devices, aiming to address issues found in previous designs such as slow heating rates, low battery efficiency, and high temperature rise of the switching devices. The optimal circuit conditions to meet the design requirements are found by taking the resonant circuit capacitance value, the wire diameter of the induction heating coil, the material and wall thickness of the heating tube as the optimization direction. The optimization results show that compared with other circuit conditions, it effectively improves the comprehensive performance of the control system. The system is able to heat the heating tube to the target temperature of 250°C in 11s under the output current of 4.6A from the battery, and the temperature rise of all NMOS is no more than 50°C after the system runs for 5min.

References

1. Kukartsev, V., et al. *Steel smelting in induction crucible furnaces with industrial frequency*. in *IOP Conference Series: Earth and Environmental Science*. 2018. IOP Publishing.

2. Phadungthin, R. and J. Haema. *Full bridge resonant inverter for non-ferrous metal induction heating application*. in *2015 IEEE PES Asia-Pacific Power and Energy Engineering Conference (APPEEC)*. 2015. IEEE.
3. Phadungthin, R. and J. Haema. *High frequency induction heating of full bridge resonant inverter application*. in *2016 International Symposium on Power Electronics, Electrical Drives, Automation and Motion (SPEEDAM)*. 2016. IEEE.
4. Smalcerz, A., et al., *Influence of the power of various types of induction furnaces on the shape of the metal bath surface.* 2021. **15**(3).
5. El-Mashad, H.M. and Z.J.F.E.R. Pan, *Application of induction heating in food processing and cooking.* 2017. **9**: p. 82-90.
6. Franco, C., et al., *Inductive sensor for temperature measurement in induction heating applications.* 2011. **12**(5): p. 996-1003.
7. Meng, L., K.W.E. Cheng, and K. Chan. *Heating performance improvement and field study of the induction cooker*. in *2009 3rd International Conference on Power Electronics Systems and Applications (PESA)*. 2009. IEEE.
8. Pijls, B., et al., *Segmental induction heating of orthopaedic metal implants.* 2018. **7**(11): p. 609-619.
9. Stauffer, P.R., T.C. Cetas, and R.C.J.I.T.o.B.E. Jones, *Magnetic induction heating of ferromagnetic implants for inducing localized hyperthermia in deep-seated tumors.* 1984(2): p. 235-251.
10. Pijls, B., et al., *Non-contact electromagnetic induction heating for eradicating bacteria and yeasts on biomaterials and possible relevance to orthopaedic implant infections:* in vitro *findings.* 2017. **6**(5): p. 323-330.
11. Lucía, Ó., et al., *Series-resonant multiinverter for multiple induction heaters.* 2010. **25**(11): p. 2860-2868.
12. Park, H.-P. and J.-H.J.I.T.o.I.E. Jung, *Load-adaptive modulation of a series-resonant inverter for all-metal induction heating applications.* 2018. **65**(9): p. 6983-6993.
13. Burdio, J.M., et al., *A two-output series-resonant inverter for induction-heating cooking appliances.* 2005. **20**(4): p. 815-822.
14. Bonert, R. and J.D.J.I.t.o.p.e. Lavers, *Simple starting scheme for a parallel resonance inverter for induction heating.* 1994. **9**(3): p. 281-287.
15. Nam, I. *Analysis and design method for parallel quasi resonant inverter in induction heating applications*. in *2018 IEEE Applied Power Electronics Conference and Exposition (APEC)*. 2018. IEEE.
16. Arslan, L. and H.J.A.S.N. Özbay, *Modelling and simulation of D-class current-fed parallel resonant inverter for induction heating system.* 2022. **1**(1): p. 106-116.
17. Kobos, W.J.r., *Impedance matching of the inverter for induction heating.* 2018. **9**: p. 1.
18. Esteve, V., et al., *Comparative analysis and improved design of LLC inverters for induction heating.* 2023. **16**(10): p. 1754-1764.
19. Esteve, V., et al., *Optimal LLC inverter design with SiC MOSFETs and phase shift control for induction heating applications.* 2021. **69**(11): p. 11100-11111.
20. Li, J., L. Wang, and Q. Sun. *Research on high-frequency induction heating load-matched based on LLC resonant circuit*. in *2014 International Power Electronics and Application Conference and Exposition*. 2014. IEEE.

 doi:10.20944/preprints202407.2474.v1

21. Kurre, M. and A.J.J.o.E.R. Banerjee, *Zero voltage switching self-oscillating PWM inverter in induction heating applications.* 2022.
22. Yachiangkam, S., et al., *Steady-state analysis of ZVS and NON-ZVS full-bridge inverters with asymmetrical control for induction heating applications.* 2015. **15**(2): p. 544-554.
23. Yongyuth, N., P. Viriya, and K. Matsuse. *Analysis of a full-bridge inverter for induction heating using asymmetrical phase-shift control under zvs and non-zvs operation*. in *2007 7th International Conference on Power Electronics and Drive Systems*. 2007. IEEE.
24. Kamli, M., S. Yamamoto, and M.J.I.T.o.I.E. Abe, *A 50-150 kHz half-bridge inverter for induction heating applications.* 1996. **43**(1): p. 163-172.
25. Lee, S.-H., et al., *Design of New Current Full-Bridge Resonant Inverter for Induction Heating System.* 2012. **26**(7): p. 59-69.
26. Płatek, M. and Z.J.E.i.e., Waradzyn, *Operation modes of full-bridge voltage-source series resonant inverter with PFM control for induction heating applications.* 2006. **25**(1): p. 58-67.
27. Lakkas, G.J.A.A., *MOSFET power losses and how they affect power-supply efficiency.* 2016. **10**(2016): p. 22-26.
28. Kimball, J.W. and P.L. Chapman. *Evaluating conduction loss of a parallel IGBT-MOSFET combination*. in *Conference Record of the 2004 IEEE Industry Applications Conference, 2004. 39th IAS Annual Meeting.* 2004. IEEE.
29. Graovac, D., M. Purschel, and A.J.I.a.n. Kiep, *MOSFET power losses calculation using the data-sheet parameters.* 2006. **1**(1).
30. Esteve, V., et al., *Enhanced pulse-density-modulated power control for high-frequency induction heating inverters.* 2015. **62**(11): p. 6905-6914.
31. Özbay, H.J.E.S. and a.I.J. Technology, *PDM-MPPT based solar powered induction heating system.* 2020. **23**(6): p. 1397-1414.
32. Wenxu, Y., J. Zhicheng, and L. Xianling. *Power control for induction heating by asymmetrical pulse density modulation*. in *2006 1ST IEEE Conference on Industrial Electronics and Applications*. 2006. IEEE.
33. Kumaraswamy, A., A. Bhattacharya, and P.K.J.E.E. Sadhu, *Dual output direct AC–AC series resonant converter for all metal induction heating system with a hybrid control technique.* 2023. **105**(3): p. 1363-1375.
34. Kwon, Y.-S., et al., *Half-Bridge Series Resonant Inverter for Induction Cooking Application with Load-Adaptive PFM Control Strategy.* 1998: p. 1018-1023.
35. Hu, J., et al., *Power control of asymmetrical frequency modulation in a full-bridge series resonant inverter.* 2015. **30**(12): p. 7051-7059.
36. Mei-lan, Z., et al., *Design of High Frequency Induction Heating Power Supply System.* 2015. **20**(1).
37. Jeong, W., et al., *Phase-shifted third harmonic modulation technique for induction heating applications to improve soft switching capability.* 2024: p. 1-11.
38. Kifune, H., Y. Hatanaka, and M.J.I.P.-E.P.A. Nakaoka, *Cost effective phase shifted pulse modulation soft switching high frequency inverter for induction heating applications.* 2004. **151**(1): p. 19-25.

 doi:10.20944/preprints202407.2474.v1